Ninth International Conference on Computational Fluid Dynamics (ICCFD9), Istanbul, Turkey, July 11-15, 2016

ICCFD9-0276

Implicit v.s. Explicit Large Eddy Simulation of Premixed Turbulent Combustion with Multi-scale Forcing

Song Zhao[1], Fabien Thiesset[1], Nicolas Lardjane[2], Ivan Fedioun[1,3], Iskender Gökalp[1]

[1] ICARE-CNRS, 1c avenue de la Recherche Scientifique, F-45071, Orléans cedex 2, France
[2] CEA, DAM, DIF, F-91297 Arpajon, France
[3] University of Orléans, 8 rue Léonard de Vinci, F-45072, Orléans cedex 2, France
Corresponding author: song.zhao@cnrs-orleans.fr

Abstract: Implicit LES (ILES), i.e. LES without any explicit subgrid modeling, and explicit LES with Thickened Flame and subgrid scale flame wrinkling models (TFLES) are performed for the numerical simulation of low-speed CH_4/air turbulent premixed combustion. An experimental Bunsen burner with multi-grid turbulent forcing is simulated using a compressible solver based on different numerical methods, ranging from 4th order central finite difference to 5th order advanced WENO schemes. Results show that TFLES with a low dissipation scheme predicts quite well the experimental flame length and flame surface density. Implicit LES with advanced WENO schemes produce a slightly shorter but realistic flame, provided the grid spacing is of order of the laminar flame thickness.

Keywords: Premixed Turbulent Combustion, Implicit LES, TFLES, WENO

Introduction

The context of this study is the optimization of premixed turbulent combustion of syngas for clean energy production. To enhance the combustion efficiency, a high turbulence level, especially in small scales, should be induced to increase the flame surface density. As shown in [1], a multi-grid generator can lead to a nearly homogeneous and isotropic turbulence (HIT) with intensity as high as 15%, compared to 3∼4% with standard single grids. The length scales characterizing the multi-scale generated turbulence are also smaller, while the turbulent kinetic energy produced is larger.

Following this idea, a Bunsen-type burner with a multi-scale grid generator has been designed and studied experimentally at our laboratory ICARE, France [2]. As sketched in figure 1(a), the multi-grid turbulence generator is constituted by 3 grids with their parameters listed in table 1. The inner diameter of the burner is $D = 25$ mm and the bulk velocity is $U_D = 3.5$ m/s. The jet exits into a vessel in which the pressure can be varied from 0.1 to 1 MPa. Both non-reacting air/air and reacting experiments have been performed. In the non-reacting experiment, a single hot-wire and a two-channel Laser Doppler Velocimetry (LDV) measurement system provide the velocity profiles along the jet axis and at the jet exit. Reacting experiments have been performed under different pressures, equivalence ratios and types of fuel. The flame measurements are carried out by Mie-scattering tomography [3]. One experiment CH_4/air flame at $p = 1$ atm and equivalence ratio $\phi = 0.8$ is located on the Borghi-Peters diagram [4] as the red dot in figure 1(b) [3].

The object of current study is to simulate this premixed flame with different LES strategies. This paper is organized as follows: governing equations of LES for premixed turbulent combustion are given in the first section; numerical methods applied in this work are illustrated in section 2; simulations for both non-reacting and reacting experiments are presented in section 3, and conclusions are drawn at the end as section 4.

Table 1: Geometrical characteristics of the multi-scale grid where d_j , M_j , σ_j and K_j stand for the holes diameter, the mesh size, the blockage ratio and the pressure drop coefficient of the j-th perforated plate [2].

Grid	d_j (mm)	M_j (mm)	σ_j	K_j
1	1.55	2	0.46	2.43
2	3.44	5	0.57	4.41
3	7.50	12.5	0.67	8.18

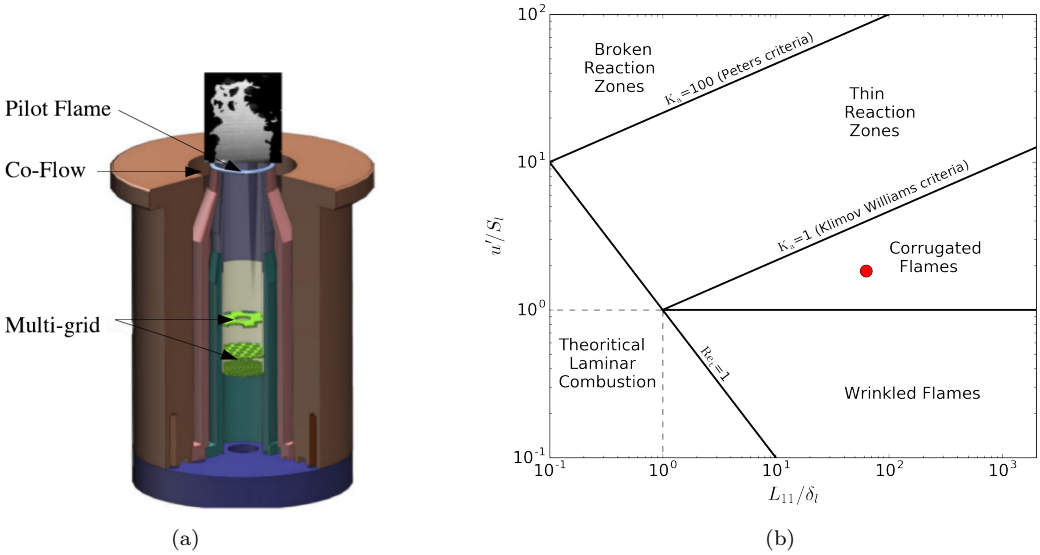

(a) (b)

Figure 1: (a) Bunsen burner with the multi-grid injection system [5]; (b) Experimental flame on the Borghi-Peters diagram ($p = 1$ atm, CH_4/air, $\phi = 0.8$)

1 Governing equations

1.1 Navier-Stokes equations

Let briefly recall the governing equations for a N_{sp} species multicomponent compressible reacting flow, the Navier-Stokes (N-S) equations. In cartesian coordinate, neglecting body forces, the conservation form of N-S equations can be written as:

$$\frac{\partial \boldsymbol{U}}{\partial t} + \frac{\partial \boldsymbol{F}}{\partial x} + \frac{\partial \boldsymbol{G}}{\partial y} + \frac{\partial \boldsymbol{H}}{\partial z} = \boldsymbol{V} + \boldsymbol{S} \tag{1}$$

where

$$\boldsymbol{U} \equiv {}^{T} \left\{ \rho, \rho u, \rho v, \rho w, \rho E, \rho Y_1, \cdots, \rho Y_{N_{sp}} \right\} \tag{2}$$

is the vector of conservative variables, with ρ the density, and u, v and w the velocity components along x, y and z directions. Y_k is the mass fraction of species k, and E is the total energy per unit mass of the mixture, defined as the sum of the internal and kinetic energy

$$E = \sum_{k=1}^{N_{sp}} \left(\Delta h_k^0 + \int_{T_0}^{T} C_{pk}(\theta) d\theta \right) Y_k - rT + \frac{1}{2} u_i u_i \tag{3}$$

The specific heat at constant pressure C_{pk} and the enthalpy of formation Δh_k^0 at temperature $T_0 = 298$ K for species k are taken from the thermodynamic database of A. Burcat and B. Ruscic [6].

• $\boldsymbol{F}$, $\boldsymbol{G}$ and $\boldsymbol{H}$ in (1) are the fluxes in x, y and z directions

$$\begin{aligned}
\boldsymbol{F} \equiv & \quad {}^T\left\{\rho u, \rho u^2 + p, \rho uv, \rho uw, \rho Eu + pu, \rho uY_1, \cdots, \rho uY_{N_{sp}}\right\} \\
\boldsymbol{G} \equiv & \quad {}^T\left\{\rho v, \rho vu, \rho v^2 + p, \rho vw, \rho Ev + pv, \rho vY_1, \cdots, \rho vY_{N_{sp}}\right\} \\
\boldsymbol{H} \equiv & \quad {}^T\left\{\rho w, \rho wu, \rho wv, \rho w^2 + p, \rho Ew + pw, \rho wY_1, \cdots, \rho wY_{N_{sp}}\right\}
\end{aligned} \tag{4}$$

where the pressure p can be obtained from the equation of state. Assuming perfect gases, it reads

$$p = \rho r T = \sum_{k=1}^{N_{sp}} \rho_k r_k T = \rho \mathcal{R} T \sum_{k=1}^{N_{sp}} \frac{Y_k}{W_k} \tag{5}$$

where $\mathcal{R} = 8.31451$ J.K^{-1}.mol^{-1} is the universal gas constant, and W_k is the molecular weight for species k.

• $\boldsymbol{V}$ in (1) represents the viscous terms

$$\boldsymbol{V} \equiv \begin{bmatrix} 0 \\ \tau_{xx,x} + \tau_{xy,y} + \tau_{xz,z} \\ \tau_{yx,x} + \tau_{yy,y} + \tau_{yz,z} \\ \tau_{zx,x} + \tau_{zy,y} + \tau_{zz,z} \\ v_5 \\ -J_{1x,x} - J_{1y,y} - J_{1z,z} \\ \vdots \\ -J_{N_{sp}x,x} - J_{N_{sp}y,y} - J_{N_{sp}z,z} \end{bmatrix} \tag{6}$$

with

$$v_5 = \left(u_i \tau_{ij}\right)_{,j} - q_{j,j} \quad \text{for } i, j = 1, 2, 3$$

τ_{ij}, q_j and J_{kj} in viscous terms stand respectively for the viscous stress, heat flux, and species mass flux. They all vanish for an inviscid fluid, giving the set of Euler equations. The viscous stress for a Stokes-Newtonian mixture reads

$$\tau_{ij} = \mu\left(u_{i,j} + u_{j,i} - \frac{2}{3} u_{l,l}\delta_{ij}\right) = \mu S_{ij} \tag{7}$$

The heat flux q_j in direction x_j in (6) results from partial enthalpies fluxes, from the Fourier law and from Dufour effect:

$$q_j = \sum_{k=1}^{N_{sp}} h_k J_{kj} - \lambda T_{,j} - p \sum_{k=1}^{N_{sp}} D_k^T d_{kj} \tag{8}$$

The mass flux J_{kj} of species k in direction x_j can be expressed using the species diffusion velocity

$$J_{kj} \equiv \rho Y_k V_{kj} \tag{9}$$

This diffusion velocity can be modeled by the sum of the Fickian diffusion velocity, the barotrope diffusion and the Soret effect[1]

$$V_{kj} = -\sum_{\beta=1}^{N_{sp}} \mathcal{D}_{k\beta}\left(X_{\beta,j} + \left(X_\beta - Y_\beta\right)\left(\ln P\right)_{,j}\right) - D_k^T \left(\ln T\right)_{,j} \tag{10}$$

In the current work, the viscosity μ of the mixture, the heat flux and the species diffusion velocity are calculated using the EGLIB library [7, 8, 9].

[1] Only the first part is considered in the current work

• $\boldsymbol{S}$ in (1) is the vector of the chemical source term

$$\boldsymbol{S} \equiv {}^{T}\left\{0,0,0,0,0,\dot{\omega}_1,\cdots,\dot{\omega}_{N_{sp}}\right\} \tag{11}$$

where $\dot{\omega}_k$ is the mass production/consumption rate of species k by chemical reactions per unit volume ($\mathrm{kg.s^{-1}.m^{-3}}$). For a chemical system that involves N_{sp} species and N_{react} reactions

$$\sum_{k=1}^{N_{sp}} \nu'_{kj} A_k \rightleftarrows \sum_{k=1}^{N_{sp}} \nu''_{kj} A_k \qquad j = 1, ..., N_{reac} \tag{12}$$

the net mass production/consumption rate of species k can be calculated as sum of the net production/consumption rate of species k in each reaction

$$\dot{\omega}_k = W_k \sum_{j=1}^{N_{reac}} \left(\nu''_{kj} - \nu'_{kj}\right) \left[K_{fj} \prod_{\beta=1}^{N_{sp}} \left(\frac{\rho Y_\beta}{W_\beta}\right)^{\nu'_{kj}} - K_{bj} \prod_{\beta=1}^{N_{sp}} \left(\frac{\rho Y_\beta}{W_\beta}\right)^{\nu''_{kj}} \right] \tag{13}$$

where K_{fj} and K_{bj} represent the forward and backward reaction rate constants for reaction j. They can be modeled with the generic Arrhénius formula

$$K = A T^b \exp\left(-\frac{E_{act}}{\mathcal{R}T}\right) \tag{14}$$

with coefficients (A, b, E_{act}) as the pre-exponential constant, the temperature exponent and the activation energy of reaction j. The forward and backward reaction rate constants are related to each other by the equilibrium constant of the j^{th} reversible reaction

$$K_{ej} = \frac{K_{fj}}{K_{bj}} = \left(\frac{P_{atm}}{\mathcal{R}T}\right)^{\sum_{k=1}^{N_{sp}} \nu''_{kj} - \nu'_{kj}} \exp\left(\frac{\Delta S_j^0}{\mathcal{R}} - \frac{\Delta H_j^0}{\mathcal{R}T}\right) \tag{15}$$

In this work, the Arrhénius coefficients (A, b, E_{act}) are inputs in CHEMKIN format [10] and the mass production/consumption rates $\dot{\omega}_k$ are evaluated using CHEMKIN or CANTERA libraries [11].

1.2 LES formalism

The LES of multi-component compressible reacting flows are performed by resolving the filtered N-S equations[12, 13, 14]. After filtering, the original N-S equations in conservation form (1) becomes

$$\frac{\partial \widehat{\boldsymbol{U}}}{\partial t} + \frac{\partial \widehat{\boldsymbol{F}}}{\partial x} + \frac{\partial \widehat{\boldsymbol{G}}}{\partial y} + \frac{\partial \widehat{\boldsymbol{H}}}{\partial z} = \widehat{\boldsymbol{V}} + \widehat{\boldsymbol{S}} + \boldsymbol{\tau} \tag{16}$$

with

$$\widehat{\boldsymbol{U}} \equiv {}^{T}\left\{\bar{\rho}, \bar{\rho}\widetilde{u}, \bar{\rho}\widetilde{v}, \bar{\rho}\widetilde{w}, \bar{\rho}\widetilde{E}, \bar{\rho}\widetilde{Y}_1, \cdots, \bar{\rho}\widetilde{Y}_{N_{sp}}\right\} \tag{17}$$

as the resolved conservative variables. The notation $\bar{\cdot}$ represents filtered variables and $\widetilde{\cdot}$ stands for Favre filtered variables [14].

• $\widehat{\boldsymbol{F}}$, $\widehat{\boldsymbol{G}}$ and $\widehat{\boldsymbol{H}}$ in equation (16) are, respectively, the resolved inviscid or Euler fluxes in x, y and z directions

$$\begin{aligned}
\widehat{\boldsymbol{F}} \equiv & \quad {}^{T}\left\{\bar{\rho}\widetilde{u}, \bar{\rho}\widetilde{u}^2 + \widehat{p}, \bar{\rho}\widetilde{u}\widetilde{v}, \bar{\rho}\widetilde{u}\widetilde{w}, \bar{\rho}\widetilde{E}\widetilde{u} + \widehat{p}\widetilde{u}, \bar{\rho}\widetilde{u}\widetilde{Y}_1, \cdots, \bar{\rho}\widetilde{u}\widetilde{Y}_{N_{sp}}\right\} \\
\widehat{\boldsymbol{G}} \equiv & \quad {}^{T}\left\{\bar{\rho}\widetilde{v}, \bar{\rho}\widetilde{v}\widetilde{u}, \bar{\rho}\widetilde{v}^2 + \widehat{p}, \bar{\rho}\widetilde{v}\widetilde{w}, \bar{\rho}\widetilde{E}\widetilde{v} + \widehat{p}\widetilde{v}, \bar{\rho}\widetilde{v}\widetilde{Y}_1, \cdots, \bar{\rho}\widetilde{v}\widetilde{Y}_{N_{sp}}\right\} \\
\widehat{\boldsymbol{H}} \equiv & \quad {}^{T}\left\{\bar{\rho}\widetilde{w}, \bar{\rho}\widetilde{w}\widetilde{u}, \bar{\rho}\widetilde{w}\widetilde{v}, \bar{\rho}\widetilde{w}^2 + \widehat{p}, \bar{\rho}\widetilde{E}\widetilde{w} + \widehat{p}\widetilde{w}, \bar{\rho}\widetilde{w}\widetilde{Y}_1, \cdots, \bar{\rho}\widetilde{w}\widetilde{Y}_{N_{sp}}\right\}
\end{aligned} \tag{18}$$

Here, the operator $\widehat{\cdot}$ denotes variables calculated directly from (Favre) filtered variables. For instance, $\widehat{p}$ is the resolved pressure

$$\widehat{p} = \overline{\rho}\widetilde{r}\widehat{T} \tag{19}$$

where the resolved temperature $\widehat{T}$ is evaluated from the Favre filtered total energy using

$$\widetilde{E} = \sum_{k=1}^{N_{sp}} \left(\Delta h_k^0 + \int_{T_0}^{\widehat{T}} C_{pk}(\theta) d\theta \right) \widetilde{Y_k} - \widetilde{r}\widehat{T} + \frac{1}{2}\widetilde{u_i}\widetilde{u_i} \tag{20}$$

- $\widehat{\boldsymbol{V}}$ is the vector of resolved viscous fluxes,

$$\widehat{\boldsymbol{V}} \equiv \begin{bmatrix} 0 \\ \widehat{\tau}_{xx,x} + \widehat{\tau}_{xy,y} + \widehat{\tau}_{xz,z} \\ \widehat{\tau}_{yx,x} + \widehat{\tau}_{yy,y} + \widehat{\tau}_{yz,z} \\ \widehat{\tau}_{zx,x} + \widehat{\tau}_{zy,y} + \widehat{\tau}_{zz,z} \\ \widehat{v}_5 \\ -\widehat{J}_{1x,x} - \widehat{J}_{1y,y} - \widehat{J}_{1z,z} \\ \vdots \\ -\widehat{J}_{N_{sp}x,x} - \widehat{J}_{N_{sp}y,y} - \widehat{J}_{N_{sp}z,z} \end{bmatrix} \tag{21}$$

with

$$\widehat{v}_5 = \left(\widetilde{u}_i \widehat{\tau}_{ij}\right)_{,j} - \widehat{q}_{j,j}$$

- $\widehat{\boldsymbol{S}}$ is the vector of resolved chemical source terms,

$$\widehat{\boldsymbol{S}} \equiv {}^T \left\{ 0, 0, 0, 0, 0, \widehat{\dot{\omega}}_1, \cdots, \widehat{\dot{\omega}}_{N_{sp}} \right\} \tag{22}$$

where the resolved mass production/consumption rates $\widehat{\dot{\omega}}_k$ are calculated using the Arrhénius formula with the resolved density, temperature and mass concentration (quasi-laminar approach).

Besides these resolved terms, the Sub-Filter Scale (SFS) term $\boldsymbol{\tau}$ also appears in the filtered N-S equations (16) because of the linear filtering operation on the non-linear N-S equations (1). It reads

$$\boldsymbol{\tau} \equiv \begin{bmatrix} 0 \\ (A_{11j} + A_{21j} + A_3\delta_{1j}), j \\ (A_{12j} + A_{22j} + A_3\delta_{2j}), j \\ (A_{13j} + A_{23j} + A_3\delta_{3j}), j \\ (B_{1j} + B_{2j} + B_{3j} + B_{4j})_{,j} \\ (C_{11j} + C_{21j})_{,j} + C_{31} \\ \vdots \\ \left(C_{1N_{sp}j} + C_{2N_{sp}j}\right)_{,j} + C_{3N_{sp}} \end{bmatrix} \tag{23}$$

with

$$\begin{array}{ll} A_{1ij} \equiv -\overline{\rho}\left(\widetilde{u_i u_j} - \widetilde{u}_i\widetilde{u}_j\right); & A_{2ij} \equiv \overline{\mu S_{ij}} - \widetilde{\mu}\widetilde{S_{ij}}; \\ A_3 \equiv \overline{\rho}\left(\widetilde{rT} - \widetilde{r}\widetilde{T}\right); & B_{1j} \equiv -\overline{\rho}\left(\widetilde{Eu_j} - \widetilde{E}\widetilde{u}_j\right); \\ B_{2j} \equiv -\left(\overline{pu_j} - \widehat{p}\widetilde{u}_j\right); & B_{3j} \equiv \overline{u_i\tau_{ij}} - \widetilde{u}_i\widehat{\tau}_{ij}; \\ B_{4j} \equiv \left(\overline{\lambda T_{,j}} - \widetilde{\lambda}\widehat{T}_{,j}\right) - \sum_{k=1}^{N_{sp}}\left(\overline{h_k J_{kj}} - \widehat{h}_k\widehat{J}_{kj}\right); & C_{1kj} \equiv -\overline{\rho}\left(\widetilde{u_j Y_k} - \widetilde{u}_j\widetilde{Y_k}\right); \\ C_{2kj} \equiv -\overline{J_{kj}} + \widehat{J}_{kj}; & C_{3k} \equiv \overline{\dot{\omega}}_k - \widehat{\dot{\omega}}_k \end{array} \tag{24}$$

These SFS terms represent the effect of scales smaller than the filter size on resolved scales. In practice, it should be modeled explicitly or can be balanced by numerical errors, leading to two different LES strategies: *explicit (physical) LES* and *implicit (numerical) LES (ILES)*.

Explicit LES with sound SFS models have been widely used and well discussed in the literature, especially for combustion simulations [4, 15, 16]. In this approach, SFS terms are modeled from resolved quantities

either functionally or structurally, as illustrated by P. Sagaut [13], and are explicitly inserted to the filtered N-S equations as extra forcing terms. The numerical errors, especially dissipative errors, should be minimized so that the impact of numerics can be neglected [12].

On the other hand, ILES aims to cancel the SFS terms by numerical errors introduced by well-chosen spatial/time numerical schemes [17, 18]. In this approach, no extra SFS forcing term appears in the governing equations, that can be written as

$$\frac{\delta \widehat{\boldsymbol{U}}}{\delta t} + \frac{\delta \widehat{\boldsymbol{F}}}{\delta x} + \frac{\delta \widehat{\boldsymbol{G}}}{\delta y} + \frac{\delta \widehat{\boldsymbol{H}}}{\delta z} = \widehat{\boldsymbol{V}} + \widehat{\boldsymbol{S}} \tag{25}$$

where the operators $\frac{\delta}{\delta x_i}(\cdot)$ and $\frac{\delta}{\delta t}(\cdot)$ stand for dissipative spatial/time numerical differential operators. Historically, this strategy is also called Monotone Integrated LES (MILES), as it may use monotone schemes [19, 20]. This approach has been successfully applied to high-speed non-premixed H_2/air combustion by our group, with dissipative shock-capturing non-linear WENO schemes [21, 22].

This work contributes to the comparison of implicit and explicit LES in the context of low speed premixed combustion. For ILES, numerics used for high-speed flows is adapted to low-Mach configurations. It will be illustrated in the next section. For physical LES, the Thickened Flame [23] and SGS wrinkling factor models (TFLES) are applied for flame modeling. The thickened flame method can catch a correct flame speed and a thickened laminar flame structure on a relatively coarse mesh by enlarging the diffusion and reducing the chemical source terms with same thickening factor $\mathcal{F}$ in the species equations

$$\frac{\partial \rho Y_k}{\partial t} + \left(\rho u_j Y_k\right)_{,j} = -\mathcal{F} J_{kj,j} + \frac{\dot{\omega}_k}{\mathcal{F}} \tag{26}$$

For a turbulent flame, a subgrid wrinkling factor Ξ should be used to recover the flame speed lost by flame thickening. It is defined as the ratio between the real and resolved turbulent flame speed [24]

$$\Xi = S_T / S_{T,\text{resolved}} \tag{27}$$

and it is applied in the species equations like

$$\frac{\partial \rho Y_k}{\partial t} + \left(\rho u_j Y_k\right)_{,j} = -\left(\mathcal{F}\Xi J_{kj}\right)_{,j} + \frac{\Xi \dot{\omega}_k}{\mathcal{F}} \tag{28}$$

This wrinkling factor should be modeled with local flow quantities to reproduce the unresolved flame/turbulence interactions. In the present study, a new SGS model proposed by F. Thiesset *et al.* [3, 5, 25] is implemented. This model, derived from [26], has the form

$$\Xi = \left\{ \left[1 + \left(\frac{\Delta_F}{\eta_i} \right)^{\alpha} \right] / \left[1 + \left(\frac{\Delta_F}{\eta_o} \right)^{\alpha} \right] \right\}^{\beta/\alpha} \tag{29}$$

where $\alpha = 2$, $\beta = D_f - 2$ as in fractal models, $\Delta_F = \mathcal{F}\delta_L^0$ is the flame filter width (δ_L^0: thermal flame thickness), $\eta_o \approx 3L_t$ is the outer length scale (L_t: integral turbulent length scale, input for the model), η_i is the inner cut-off length-scale, related to the local Karlovitz number $\mathrm{K_a} \equiv \tau_c/\tau_k$

$$\frac{\eta_i}{\delta_L^0} = {\mathrm{K_a}}^{-2} + r_1^* {\mathrm{K_a}}^{-1/2} \quad ; \quad r_1^* = (3C_q)^{3/4} \tag{30}$$

with $C_q = \frac{11}{3} C_u$, $C_u \approx 2$ being the "universal" constant in Kolmogorov's 2/3 law. The first term on the r.h.s. of (30) accounts for low Karlovitz numbers, whereas the second one accounts for high $\mathrm{K_a}$. The expression for β in (29) slightly differs from the one of [27], and reads

$$3\beta = 1 + \frac{r_1^* {\mathrm{K_a}}^{-1/2}}{{\mathrm{K_a}}^{-2} + r_1^* {\mathrm{K_a}}^{-1/2}} \tag{31}$$

The main difficulty is to estimate the local Karlovitz number from the resolved field. Different expressions

for $\mathrm{K_a}$ are

$$\mathrm{K_a} = \mathrm{Sc}\left(\frac{\delta}{\eta}\right)^2 = \mathrm{Sc}^{-1}\left(\frac{u_K}{S_L^0}\right)^2 = \frac{\sqrt{\varepsilon/\nu_u}}{S_L^0/\delta} \tag{32}$$

where δ is the diffusive thickness of the flame such that $\mathrm{Re}_f = \delta S_L^0/\nu_u = 1$, u_K is the Kolmogorov velocity scale, and $\mathrm{Sc} = \nu_u/D_{fuel\to air}$ is the Schmidt number usually assumed close to unity. The last expression for $\mathrm{K_a}$ in (32) can be used if a value is given to the turbulent kinetic energy dissipation rate ε. This can be achieved from

$$\varepsilon = C_\varepsilon \frac{k_{sgs}^{3/2}}{\Delta} \approx C_\varepsilon \frac{u_\Delta^3}{\Delta} \quad ; \quad C_\varepsilon = 1.05 \tag{33}$$

where Δ and u_Δ are the a length scale and velocity fluctuation at scale Δ, respectively. One possibility is to compute ε from the subgrid scale eddy-viscosity[2] ν_{sgs}^t

$$\varepsilon = {\nu_{sgs}^t}^3/(C_s\Delta)^4 \tag{34}$$

with $C_s = 0.18$ and $\Delta \equiv h = (\Delta x \Delta y \Delta z)^{1/3}$. The subgrid scale eddy-viscosity in (34) can be evaluated from flow SGS models, e.g., by the Smagorinsky model [28].

Another method to evaluate the turbulent dissipation rate ε is to calculate u_Δ with the operator OP_2 proposed by Colin *et al.* [24]. This operator estimates the turbulent velocity u_Δ without the impact of the thermal expansion near the flame front. A detailed formulation of this operator can be found in [24].

2 Numerics

As mentioned before, numerics is important for both implicit and explicit LES. In this section, numerical methods for spatial and time discretization used in this work are illustrated and applied to two simple academic test-cases to verify our numerical setup.

2.1 Numerical Schemes

Characteristic-wise Finite Difference (FD) schemes with flux-splitting are applied for spatial derivatives, and time stepping is achieved by a 3rd order TVD Runge-Kutta (R-K) method [29].

Take the flux on the x direction $\frac{\delta\widehat{\boldsymbol{F}}}{\delta x}$ as an example. Fluxes on y and z direction ($\frac{\delta\widehat{\boldsymbol{G}}}{\delta y}$ and $\frac{\delta\widehat{\boldsymbol{H}}}{\delta z}$) can be evaluated following similar processes. The FD method for conservation laws evaluates the flux at node $x = x_i$ with the flux values at node intercells $x = x_{i\pm1/2}$ as

$$\left.\frac{\delta\widehat{\boldsymbol{F}}}{\delta x}\right|_i \equiv \frac{\boldsymbol{F}_{i+1/2} - \boldsymbol{F}_{i-1/2}}{\Delta x} \tag{35}$$

where Δx is the grid spacing. As all variables appearing in the sequel of this section are resolved variables, the filtering symbols $\widehat{\cdot}$, $\bar{\cdot}$ and $\widetilde{\cdot}$ will be neglected without misunderstanding. The intercell value of flux, $\boldsymbol{F}_{i\pm1/2}$ in the R.H.S. of equation (35), is evaluated with a flux splitting in the characteristic space

$$\boldsymbol{F}_{i\pm1/2} = \boldsymbol{F}^+_{i\pm1/2} + \boldsymbol{F}^-_{i\pm1/2} \tag{36}$$

where

$$\boldsymbol{F}^+_{i+1/2} \equiv \frac{1}{2} R_{i+1/2}\left(\sum_{j=-n}^{m} a^+_{+j}\left(R^{-1}_{i+1/2}\boldsymbol{F}_{i+j} + |\Lambda|_{max} R^{-1}_{i+1/2}\boldsymbol{U}_{i+j}\right)\right)$$

$$\boldsymbol{F}^-_{i+1/2} \equiv \frac{1}{2} R_{i+1/2}\left(\sum_{j=-n}^{m} a^-_{+j}\left(R^{-1}_{i+1/2}\boldsymbol{F}_{i+j} - |\Lambda|_{max} R^{-1}_{i+1/2}\boldsymbol{U}_{i+j}\right)\right)$$

[2]Simply according to $v_{sgs}^t \sim ul$ and $\varepsilon \sim u^3/l$.

$$\boldsymbol{F}^{+}_{i-1/2} \equiv \frac{1}{2} R_{i-1/2} \left(\sum_{j=-n}^{m} a^{+}_{-j} \left(R^{-1}_{i-1/2} \boldsymbol{F}_{i+j} + |\Lambda|_{max} R^{-1}_{i-1/2} \boldsymbol{U}_{i+j} \right) \right)$$
$$\boldsymbol{F}^{-}_{i-1/2} \equiv \frac{1}{2} R_{i-1/2} \left(\sum_{j=-n}^{m} a^{-}_{-j} \left(R^{-1}_{i-1/2} \boldsymbol{F}_{i+j} - |\Lambda|_{max} R^{-1}_{i-1/2} \boldsymbol{U}_{i+j} \right) \right) \tag{37}$$

The matrix R and R^{-1} are the matrix of right and left eigenvectors of the Jacobian

$$A \equiv \frac{\partial \boldsymbol{F}}{\partial \boldsymbol{U}} = R \Lambda R^{-1} \tag{38}$$

and Λ is the diagonal matrix composed by all eigen values of the Jacobian matrix A. These matrix can be obtained analytically from local conservative variables as listed in appendix. In equation (37), the matrix $R_{i\pm1/2}$ and $R^{-1}_{i\pm1/2}$ represent the matrix on the intercell $x = x_{i\pm1/2}$. They are calculated from the intercell conservative variable $\boldsymbol{U}_{i\pm1/2}$, which can be calculated by either a simple mean of two neighbor cell values or by a Roe average [30]. $|\Lambda|_{max}$ in (37) is the maximum absolute value of Λ in the whole calculation domain Ω

$$|\Lambda|_{max} = \max_{\Omega} (|\Lambda|) \tag{39}$$

In equation (37), $a^{\pm}_{\pm_j}$ are the coefficients to reconstruct the intercell values using polynomial interpolation. For linear FD schemes, these coefficients are constant, as listed in table 2 for some classical linear schemes. For non-linear shock-capturing schemes, in order to minimize the oscillations near discontinuities caused by polynomial interpolation, these coefficients $a^{\pm}_{\pm_j}$ should be calculated using local flux values instead of kept constant. This procedure has been well illustrated in [29] for the classic WENO-JS scheme, and in [31, 32, 22] for improved WENO-M, WENO-Z and WENO-MZ schemes, respectively.

In fact, a combination of two sets of coefficients $a^{\pm}_{\pm_j}$ is still a valid set for intercell value reconstruction. This will be particularly interesting for low speed applications where central schemes and upwind schemes can be combined together to reduce the dissipative errors [33]. In the current work, a hybrid central-upwind method with a combination of 4th order central (4C) and 5th order upwind (UP5) schemes is applied. Coefficients $a^{\pm}_{\pm_j}$ for this hybrid scheme read:

$$a^{\pm}_{\pm_j,\mathrm{HYB}} = \theta \cdot a^{\pm}_{\pm_j,\mathrm{UP5}} + (1-\theta) \cdot a^{\pm}_{\pm_j,\mathrm{4C}} \tag{40}$$

with $0 \leq \theta \leq 1$. In practice, we found that a value of θ like 1% is already enough to lead to a stable low-dissipative simulation. More discussion on this scheme can be found in the test-cases presented hereafter.

The 3rd order explicit TVD R-K scheme [29] reads:

$$\begin{aligned}
\widehat{\boldsymbol{U}}^{(1)} &= \widehat{\boldsymbol{U}}^{n} + \Delta t \cdot \mathcal{NL}(\widehat{\boldsymbol{U}}^{n}) \\
\widehat{\boldsymbol{U}}^{(2)} &= \frac{3}{4}\widehat{\boldsymbol{U}}^{n} + \frac{1}{4}\widehat{\boldsymbol{U}}^{(1)} + \frac{1}{4}\Delta t \cdot \mathcal{NL}(\widehat{\boldsymbol{U}}^{(1)}) \\
\widehat{\boldsymbol{U}}^{n+1} &= \frac{1}{3}\widehat{\boldsymbol{U}}^{n} + \frac{2}{3}\widehat{\boldsymbol{U}}^{(2)} + \frac{2}{3}\Delta t \cdot \mathcal{NL}(\widehat{\boldsymbol{U}}^{(2)})
\end{aligned} \tag{41}$$

where $\widehat{\boldsymbol{U}}^{n}$ and $\widehat{\boldsymbol{U}}^{n+1}$ represent the resolved conservative variables at time step n and $(n+1)$. The operator $\mathcal{NL}(\cdot)$ includes the inviscid fluxes (18), viscous terms (21) and source terms (22). The time step Δt is generally constrained by the Courant–Friedrichs–Lewy (CFL) condition and chemical constrains for reacting flows.

For low speed applications, this explicit time stepping is not efficient because of the too small time steps given by the CFL condition. The Artificial Acoustic Reduction (ASR) method introduced by Wang and Trouvé [34] is applied in this work to enlarge the time step by reducing the speed of sound artificially. This

Table 2: Coefficients $a^{\pm}_{\pm_j}$ in equation (37) for some classical linear schemes.

	j	-3	-2	-1	0	1	2	3
2nd order Central	$a^{+}_{+_j}$	0	0	0	1/2	1/2	0	0
	$a^{-}_{+_j}$	0	0	0	1/2	1/2	0	0
	$a^{+}_{-_j}$	0	0	1/2	1/2	0	0	0
	$a^{-}_{-_j}$	0	0	1/2	1/2	0	0	0
4nd order Central	$a^{+}_{+_j}$	0	0	-1/12	7/12	7/12	-1/12	0
	$a^{-}_{+_j}$	0	0	-1/12	7/12	7/12	-1/12	0
	$a^{+}_{-_j}$	0	-1/12	7/12	7/12	-1/12	0	0
	$a^{-}_{-_j}$	0	-1/12	7/12	7/12	-1/12	0	0
5th order Upwind	$a^{+}_{+_j}$	0	1/30	-13/60	47/60	9/20	-1/20	0
	$a^{-}_{+_j}$	0	0	-1/20	9/20	47/60	-13/60	1/30
	$a^{+}_{-_j}$	1/30	-13/60	47/60	9/20	-1/20	0	0
	$a^{-}_{-_j}$	0	-1/20	9/20	47/60	-13/60	1/30	0

method only modifies the total energy equation in N-S equations

$$\frac{\partial \rho E}{\partial t} + \left[(\rho E + p)\, u_j \right]_{,j} - F_{ASR} = \left(u_i \tau_{ij} \right)_{,j} - q_{j,j} + V_{ASR} \tag{42}$$

where

$$F_{ASR} \equiv \left(1 - \frac{1}{\alpha^2} \right) \frac{\gamma p}{\gamma - 1} \frac{\partial u_j}{\partial x_j} \tag{43}$$

is the Euler part of the additional term of the ASR method to reduce the eigenvalues of the Jacobian matrix. In (43), α is the speed-up ratio to reduce the speed of sound α times artificially. The viscous and source correction term V_{ASR} for multi-species reacting flows reads:

$$V_{ASR} \equiv - \left(1 - \frac{1}{\alpha^2} \right) \left[\tau_{ij} \frac{\partial u_i}{\partial x_j} - \frac{\partial q_j}{\partial x_j} - \sum_{k=1}^{N_{sp}} \left(h_k - \frac{W c_p T}{W_k} \right) \left(- \frac{\partial}{\partial x_j} (\rho Y_k V_{k,j}) + \dot{\omega}_k \right) \right] \tag{44}$$

It is clear that the Euler part F_{ASR} is not in conservation form, hence can not be incoroporated directly in the flux (18). To overcome this difficulty, an original treatment is proposed. To calculate the spatial flux in x direction with ASR, the same procedure as in equations (35) to (37) is considered except that the reconstruction of intercell values with flux-splitting is now

$$\boldsymbol{F}^{\pm}_{i\pm 1/2} \equiv \frac{1}{2} R_{i+1/2} \left(\sum_{j=-n}^{m} a^{+}_{+_j} \left(R^{-1}_{i+1/2} \left[\boldsymbol{F}_{i+j} - \boldsymbol{F}^{ASR}_{i+j} \right] + |\Lambda|_{max} R^{-1}_{i+1/2} \boldsymbol{U}_{i+j} \right) \right) \tag{45}$$

with

$$\boldsymbol{F}^{ASR}_{i+j} \equiv \begin{pmatrix} 0 \\ 0 \\ 0 \\ 0 \\ \left(1 - \frac{1}{\alpha^2} \right) \frac{\gamma p_i u_j}{\gamma - 1} \\ 0 \\ \vdots \\ 0 \end{pmatrix} \tag{46}$$

The matrix R, $|\Lambda|_{max}$ and R^{-1} should be evaluated with the speed-up ratio α as in equations (56) to (58) in the appendix. One can find that in (46), the pressure value is kept at $x = x_i$ so that the non-conservative term F_{ASR} in equation (43) can be recovered after this treatment.

2.2 Test-cases

Self decaying Homogeneous Isotropic Turbulence (HIT) and 1D laminar premixed flame are relevant test-cases to evaluate our numerical methods with respect to turbulence modeling and premixed combustion respectively.

HIT decaying

The numerical setup of this case is very classic: in a 3D calculation box $[-L/2, L/2]^3$, a HIT field is generated and used as initial condition. Periodic boundary conditions are applied on all boundaries.

In this test case, the calculation domain is fixed at $L = 60$ mm and is discretized with $N = 120$ points in each direction so that the grid size is $\Delta = 0.5$ mm. The initial HIT field is generated from hot-wire measurements of the non-reacting multi-grid experiments under $p = 1$ atm at the jet exit. The experimental 1D spatial spectrum F_{11} is firstly obtained from one-point velocity time series provided by hot-wire data, following local Taylor hypothesis. Then, the 3D experimental spectrum $E(K)$ can be obtained as [12, 35]:

$$E(K) = \frac{1}{2}K^3 \frac{d}{dK}\left(\frac{1}{K}\frac{dF_{11}(K)}{dK}\right) \tag{47}$$

A velocity field following this spectrum can be generated in Fourier space as:

$$\hat{u}_i(\vec{K}) = j_c K_j \epsilon_{ijk}\left(\delta(0)\frac{E(K)}{4\pi K^4}\right)^{\frac{1}{2}} e^{j_c\theta_i} \tag{48}$$

where θ_i is a random angle in $[0, 2\pi]$, and $j_c^2 = -1$. After FFT, a velocity field having the experimental spectrum can be obtained and used as initial field in physical space. Different LES strategies are compared in this test-case. They are setup as:

1. Explicit LES. The numerical scheme for Euler flux evaluation is 4th order central scheme without any numerical dissipation. The Smagorinsky (SM) (simulation 4C-SM-NR, NR for Non-reacting) and Selective Structure Function (SSF) [36] (4C-SSF-NR) SGS eddy-viscosity models are implemented. The parameters of the models used in this work can be found in [21].

2. Implicit LES. The Euler flux are calculated using 5th order upwind scheme (UP5-NR), hybrid central-upwind scheme with 1% upwind ($HYB_{0.01}$-NR) or with 3% upwind ($HYB_{0.03}$-NR).

Time evolution of turbulent kinetic energy $k(t) \equiv \frac{1}{2}\langle u_i u_i\rangle$ normalized by the initial kinetic energy for different simulations is displayed in figure 2. It is clear that, on this mesh, ILES with 5UP-NR is more dissipative than the explicit Smagorinsky and the SSF models. ILES with the hybrid scheme is quite similar to explicit LES with the SSF model. The 3D energy spectra $E(K, t)$ from different simulations at $t = 4$ ms are displayed in figure 3, together with the initial spectrum. The green curves display the experimental initial spectrum as a reference. An evident difference between the energy spectrum from physical LES and ILES is that explicit LES maintains small scales until the Nyquist cut-off $K = 60K_L$, whereas these small scales in ILES are damped to very small values. In the UP5-NR simulation, as in Fig. 3(d), the small scales with wave numbers larger than $10K_L$, i.e. scales smaller than 12Δ, have already been damped by the upwind scheme. The ILES $HYB_{0.01}$-NR and $HYB_{0.03}$-NR schemes can preserve small eddies up to a wave number range from $30K_L$ to $40K_L$, i.e. 3$\sim$4 Δ.

1D laminar premixed flame

A 1D laminar premixed flame is simulated with and without the thickened flame model using different numerical schemes to evaluate our numerics in the context of premixed combustion. This test case is set up as follows: on a 1D domain $x \in [-L/2, L/2]$ with $L = 20$ mm, a methane/air premixed flame at equivalence

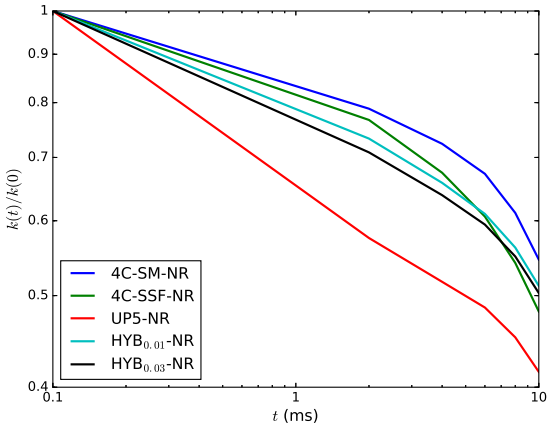

Figure 2: Time evolution of the turbulent kinetic energy with different LES strategies.

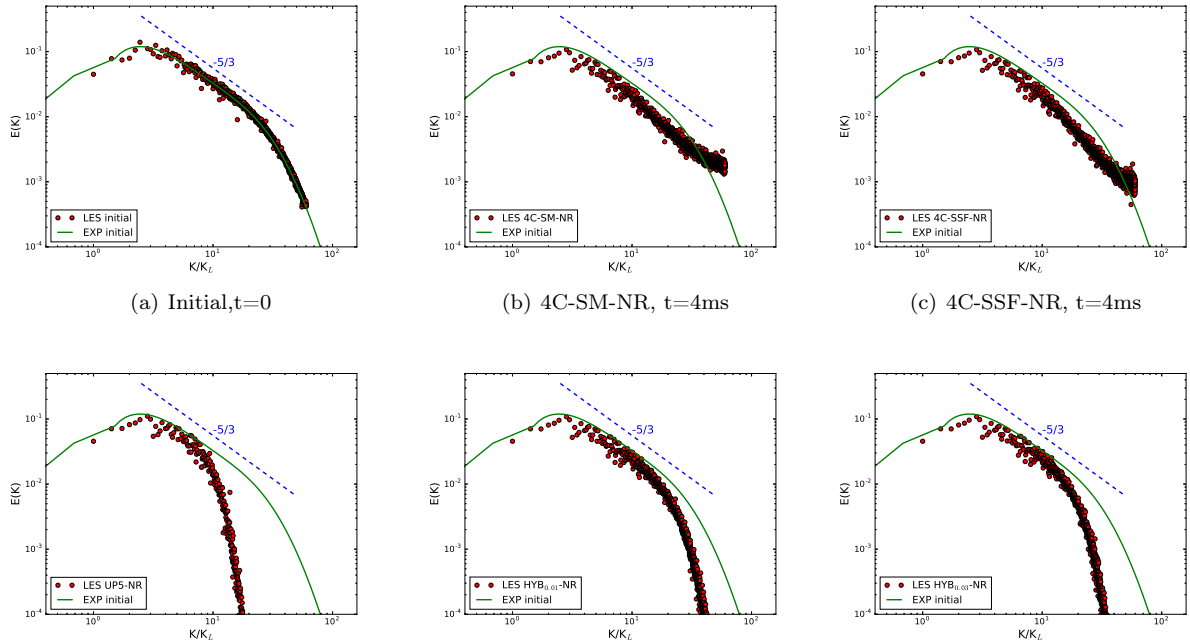

(a) Initial,t=0 (b) 4C-SM-NR, t=4ms (c) 4C-SSF-NR, t=4ms

(d) UP5-NR, t=4ms (e) HYB$_{0.01}$-NR, t=4ms (f) HYB$_{0.03}$-NR, t=4ms

Figure 3: 3D Energy spectrum at t=4 ms obtained from different LES strategies. The x axis is normalized by $K_L = 2\pi/L_x$. The Nyquist cut-off is at $K/K_L = 60$.

ratio $\phi = 0.8$ is calculated. At $t = 0$, the flow velocity and pressure field are uniform at $u_{initial} = 0.5$ m/s, $p = 1$ atm. Other quantities on the left ($x < 0$) and right ($x > 0$) half of the domain are set to fresh and burnt gas conditions with a sinus-shape profile between them to prevent sharp discontinuities. Simulations are performed on a uniform mesh, but different grid sizes might be used. The left boundary condition is set to be SI-2 NSCBC in [4] where the velocity, density and chemical components are imposed constant at $x = -L/2$. The right boundary condition is set to perfectly non reflecting outflow with NSCBC strategy. A single step methane-air chemical mechanism [15] is applied for the chemical source terms. During the calculation, the velocity of the whole domain is adjusted by the difference between the inlet speed $u(x)|_{x=-L/2}$ and the

instantaneous flame speed $S_L^0(t)$ every 0.2 ms with $S_L^0(t)$ calculated from the methane burning rate as

$$S_L^0 = -\frac{1}{\rho_f Y_{\mathrm{CH_4}}^f} \int_{-\infty}^{+\infty} \dot{\omega}_{\mathrm{CH_4}} dx \tag{49}$$

An almost steady flame structure is achieved after some times when the inlet speed becomes almost invariant thus equals to the calculated flame speed. Then, the calculated laminar flame speed is the inlet speed $u(x)|_{x=-L/2}$, and the calculated thermal flame thickness is

$$\delta_L^0 \equiv \frac{T_b - T_f}{\max\left|\frac{\partial T}{\partial x}\right|} \tag{50}$$

Reference values of flame speed and thickness can be obtained with a DNS on a very fine mesh. One finds $S_L^0 \approx 0.286$ m/s and $\delta_L^0 \approx 0.5$ mm. They are quite close to the results in the literature.

This flame is firstly calculated using the quasi-laminar approach for chemical source terms with different numerical schemes for flux evaluation, corresponding to ILES in this work. Schemes WENO-JS5 (simulation JS5-QL), WENO-MZ5 (MZ5-QL) and WENO-OPT5 (UP5-QL) have been applied. The calculated flame speed and thickness obtained from different schemes and different grid sizes are plotted in figure 4(a) and 4(b). One may find that the non-linear JS5-QL and MZ5-QL schemes can lead to stable simulations on a very coarse mesh, even with a grid size equal to the flame thickness ($\delta_L^0/\Delta x = 1$), 0.5 mm. However, the resulting flame speed and thickness at this resolution are 3∼5 times larger than the reference values and we also spotted that the flow near the flame front is quite oscillatory. The linear UP5-QL scheme is not stable until the grid size is smaller than 1/4 of the reference flame thickness, 0.125 mm. Hence, there should be at least four points inside the flame front. However, the flame speed and thickness obtained by UP5-QL are always close to the reference results. All simulations converge to reference results, when there are at least 8 points in one flame thickness.

The artificial thickened flame model is also tested, corresponding to TFLES in this work. This group of test-cases are performed on a fixed grid size $\Delta x = \delta_L^0 = 0.5$ mm with the thickening factor $\mathcal{F}$ varying from 4 to 12 (simulations UP5-$\mathrm{TF_4}$, UP5-$\mathrm{TF_6}$, UP5-$\mathrm{TF_8}$, UP5-$\mathrm{TF_{10}}$ and UP5-$\mathrm{TF_{12}}$). The resulting flame speed and thickness are displayed in figure 4(c) and 4(d). The flame speed obtained with different thickening factors is almost constant, while the flame thickness is artificially thickened $\mathcal{F}$ times.

The ASR method is also tested in this test case. It can lead to stable simulations when there is at least 8 points inside one (thickened) flame thickness, and the resulting flame is quite close to the non-ASR calculations. But in fact, for premixed combustion, even with a one-step chemical mechanism, the time step is mainly constrained by the stiffness of chemistry instead of CFL condition. So, the ASR method can not speed up this simulation.

These two academic test-cases confirm our numerical strategies in turbulence and premixed flame handling. As one can see in the HIT case, explicit LES with explicit SGS models show no clear advantage compared to ILES, so in the simulation for the experimental burner, which will be presented in the next section, even the TFLES will be performed with implicit turbulence modeling, i.e. with dissipative hybrid schemes instead of extra SGS terms for the flow part. The 1D laminar premixed flame test case shows that only WENO-JS and WENO-MZ schemes can lead to a stable flame on a relatively coarse LES mesh, so they will be used in the ILES of the experiment burner, although the laminar flame speed and thickness with this approach in 1D flame are evidently larger than the reference values.

3 Simulation of the experiment

The non-reacting and reacting experiments with multi-scale turbulent forcing are simulated in this section with the numerical methods proposed before, and the results are compared with the experimental data.

3.1 Non-reacting case

The ILES of non-reactive experiments are first performed to reproduce the experimental flow field. This simulation corresponds to the multi-grid turbulent air/air experiment running at $p = 0.1$ MPa.

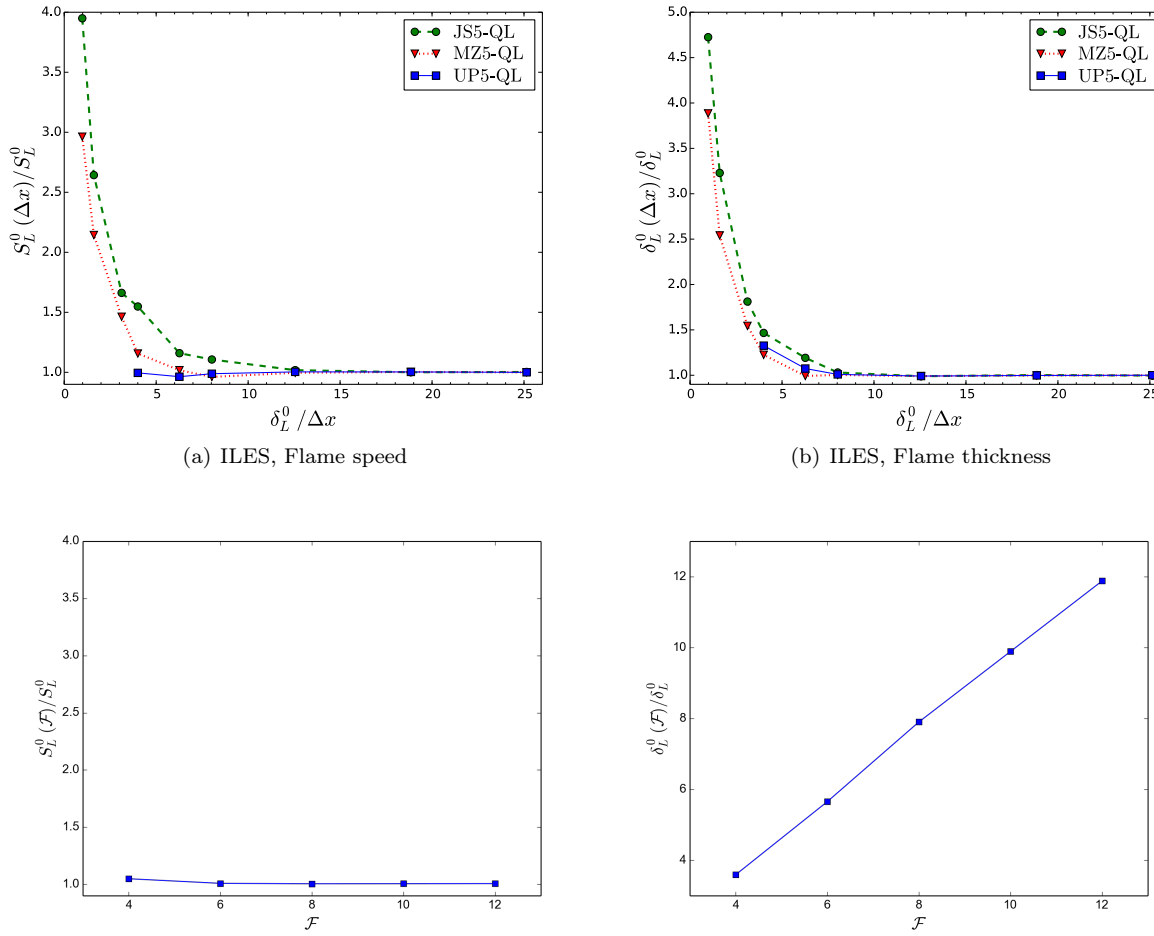

(a) ILES, Flame speed

(b) ILES, Flame thickness

(c) TFLES, Flame speed

(d) TFLES, Flame thickness

Figure 4: Calculated flame speed (left) and thermal flame thickness (right) with different numerical setup. (a),(b): ILES with different grid sizes Δx; (c),(d): TFLES with different thickening factor ($\mathcal{F}$). Results are normalized by reference flame speed $S_L^0 = 0.286$ m/s and reference flame thickness $\delta_L^0 = 0.50$ mm.

In this simulation, the same block of "synthetic" HIT field generated from experimental hot-wire measurements as in HIT test case is injected into the calculation domain with the experimental mean velocity profile, as shown in figure 5. The whole domain is set at pressure $p = 0.1$ MPa and temperature T =300 K at initial time. The outlet boundary at $x = L_x$ is set to be NSCBC in-out boundary condition with a superimposed pressure at infinity $p = 0.1$ MPa (B.C. B3 in table 9.4 of [4]); Lateral boundaries in y and z directions are set to slip-walls using the symmetric ghost points method; The boundary $x = 0$ is set to constant temperature non-slip wall using the NSCBC method at T =300 K except that at the jet exit, the boundary is set to inject the HIT field. This boundary is achieved with a NSCBC strategy adapted from the classic SI-2 NSCBC boundary condition in [4].

Two groups of simulations have been performed. Simulation Group I (G-I) is performed on a fine grid ($\Delta x \approx 3.3\eta$) with WENO-JS scheme (JS5-NR) to capture the statistical results; Group II (G-II-1 and G-II-2) uses the same setup as in the reactive simulations in order to guarantee that the flow properties in reactive case are well resolved. Details of numerical configurations are given in table 3. The ASR low-Mach formulation [34] presented before is applied to all of these simulations with a speed-up ratio $\alpha = 10$.

The result of simulation G-I confirms that our numerical strategy can be successfully applied to this non-reactive low-speed configuration. Figure 6 shows the structure of the flow with the Q-criterion iso-surface

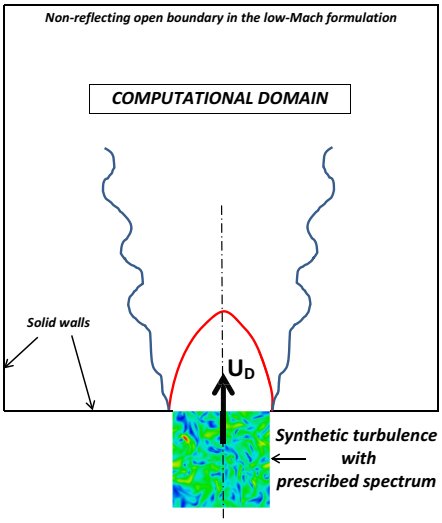

Figure 5: Sketch of the 3D multi-scale forcing simulation setup.

Table 3: Mesh and numerical parameters of the 3D non-reacting simulations.

	G-I	G-II-1	G-II-2
$L_x \times L_y \times L_z$(m)	0.2×0.1×0.1	0.3×0.3×0.3	0.3×0.3×0.3
$N_x \times N_y \times N_z$	540×200×200	240×170×170	240×170×170
Total grid points	21.6×10^6	6.9×10^6	6.9×10^6
Points in jet ∅	100	50	50
$\Delta x_{min}/\eta$	3.3	6.7	6.7
α_{ASR} - CFL	10 - 0.8	10 - 0.8	10 - 0.8
Δt (s)	0.8×10^{-5}	1.33×10^{-5}	1.33×10^{-5}
Numerical scheme	JS5-NR	MZ5-NR	$HYB_{0.03}$-NR

($Q = 1000$ s^{-2}) colored by velocity magnitude. One can see, in the center, the injected turbulent field that evolves independently from the Kelvin-Helmholtz structures arising from the inflectional instability of the jet. The inner structures in Fig. 6 indicate a fast decay of the HIT (the Taylor micro-scale increases downstream) in the potential core (length ≈ 3D). Further downstream, the breakdown to turbulence combines with the residual HIT to create a low-speed turbulent plume.

Simulations G-II-1 and G-II-2 are performed with the same numerical setup as the 3D ILES and TFLES reactive cases to validate the flow field in reactive configurations. The only difference between these two simulations is that G-II-1 is calculated with the 5th order WENO-MZ (MZ5-NR), while G-II-2 uses the hybrid central-upwind scheme with 3% of upwind ($HYB_{0.03}$-NR). An inner view of Q-criterion iso-surfaces of both simulations is displayed in figure 7 ,and the vorticity magnitude on the jet axial cut-plane is plotted in figure 8. These figures show that simulation G-II-2 with the hybrid central-upwind scheme can resolve more small scale structures than the WENO-MZ scheme does, although similar large scale structures are captured by both simulations.

The statistics of velocity and resolved turbulent kinetic energy on the jet axis are plotted in figure 9 and 10, in comparison with experimental data from [2]. Simulation G-I on the fine mesh with the WENO-JS scheme gives statistical results quite close to the experiment. Although the axial energy decay is much faster than in the experiment, the length of the potential core, where production is negligible, and the axial velocity decay are both quite well predicted. For simulation G-II-1 and G-II-2 on the coarse mesh, the axial velocity decay after $x > 3D$ is not as good as in G-I, where a finer mesh is used. In fact, in reactive experiments, the flame length is only about 3 times the jet diameter, so that these downstream velocity results should be acceptable for the reacting simulations. Meanwhile, one may find in figure 10 that, the kinetic energy

resolved by $HYB_{0.03}$-NR is even better than in the fine mesh simulation G-I with JS5-NR, and is very close to the experimental data.

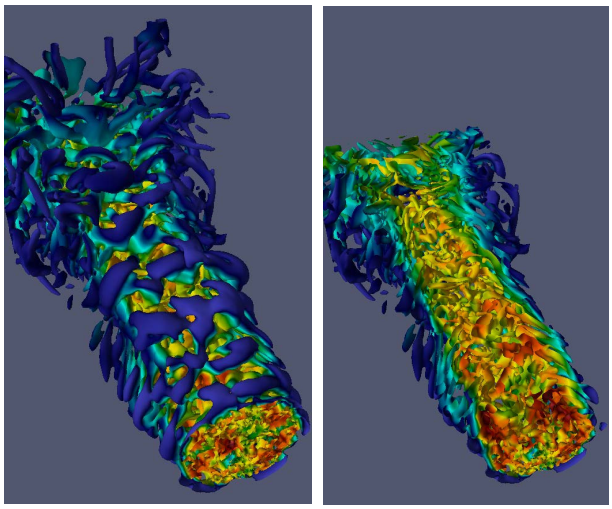

Figure 6: Q-criterion iso-surface $Q = 1000\ s^{-2}$ at $t = 0.14$ s (colored by velocity magnitude) near the injection (left), and detail of the inner structure of the jet (right) for simulation G-I.

3.2 Reacting case

The reactive experiments are now simulated with both ILES and TFLES. A CH_4/air flame at equivalence ratio $\phi = 0.8$ under p=0.1 MPa is simulated with 2D and 3D configurations. Detailed numerical setup and results are presented hereafter.

2D simulations

In fact, the experimental flame are naturally 3D, so one can not expect good statistical results from 2D simulations. In this work, 2D simulations are mainly used to assess our reacting strategy, especially SGS models for combustion in TFLES.

The mesh, boundary and initial conditions are similar to the 3D non-reactive simulations G-II before. The grid size is constant at $\Delta x = 0.5$ mm$\approx \delta_L^0$ in the flame region. The CH_4/air mixture at equivalence ratio $\phi = 0.8$ is injected into the calculation domain at bulk velocity $U_D = 3.5$ m/s, with the pre-generated HIT field from the experiment. For this 2D case, only one slice of the 3D HIT domain is used, and the velocity is scaled to enforce the same turbulent kinetic energy.

ILES simulations are quite straight-forward using this setup. A snapshot of the vorticity field resolved by WENO-MZ and quasi-laminar approach (MZ5-QL) is displayed in figure 11(a). One may find that the injected turbulence, especially the small scales, is dissipated in the fresh gas, and that near the flame, the vorticity field is quite oscillatory.

However, the TFLES is not that simple to achieve. Both numerical schemes and methods to evaluate the SGS wrinkling factor should be carefully chosen. The SGS wrinkling factor evaluated with different setups is displayed in figure 12. In Fig. 12(a), the wrinkling factor evaluated by the turbulence dissipation rate ε obtained from Smagorinsky SGS eddy-viscosity as in equation (34), is almost 1 in the fresh gas but very large near the flame front. This is clearly due to thermal expansion. So, the usage of operator OP_2 in [24] is mandatory to eliminate the impact of thermal expansion. In Fig. 12(b), the wrinkling factor calculated with OP_2 and the 5th order upwind scheme is almost 1 both in the fresh gas and near the flame front. This is because the small turbulent scales necessary to model the SGS wrinkling (from δ_L^0 to $2\mathcal{F}\delta_L^0$ [24]) are damped by the 5th order upwind scheme on this mesh, as shown in the HIT test-case and in the vorticity field in figure 11(b). To maintain these small scales, the less dissipative hybrid central-upwind scheme should

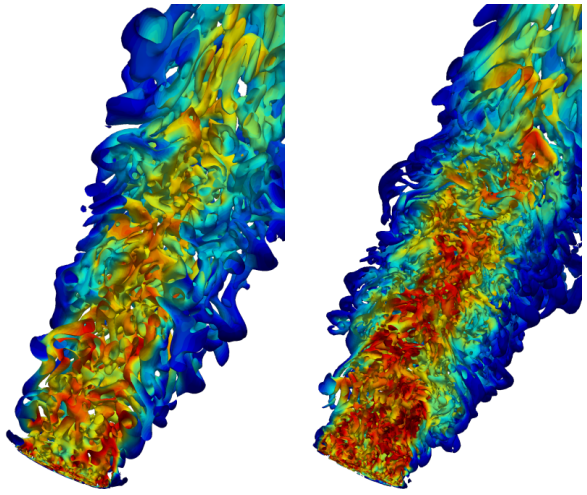

(a) G-II-1 (b) G-II-2

Figure 7: Q-criterion iso-surface (Q =1000 s^{-2}) for non-reactive simulations Group II at $t = 0.6$ s, colored by velocity magnitude. Half of the domain is displayed for a inner view.

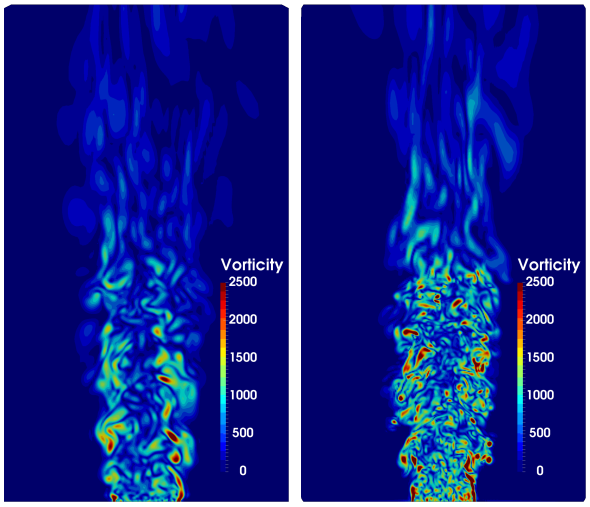

(a) G-II-1 (b) G-II-2

Figure 8: Vorticity field (1/s) on the axial cut-plane for non-reactive simulations Group II at $t = 0.6$ s.

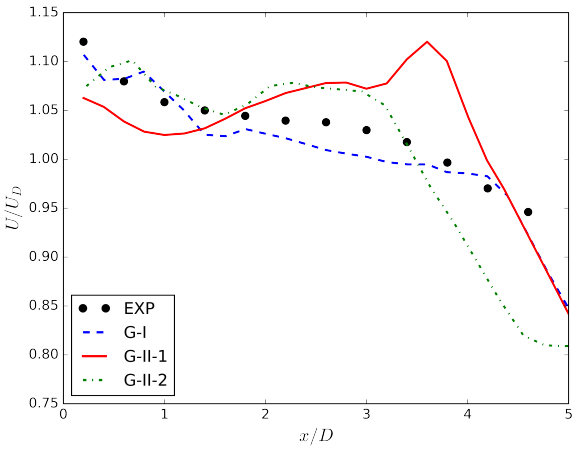

Figure 9: Evolution of the mean axial velocity on the jet axis for 3D non-reactive simulations.

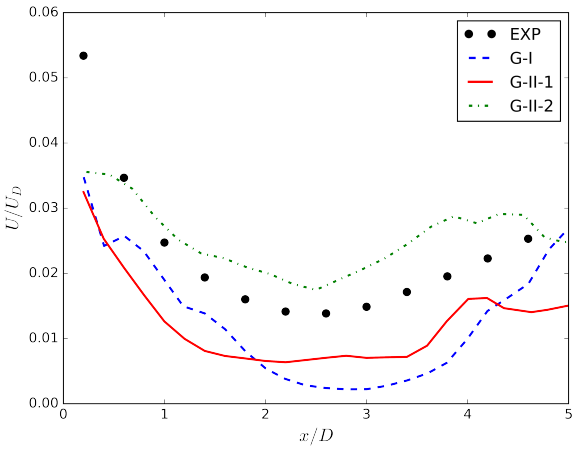

Figure 10: Evolution of the resolved turbulent kinetic energy on the jet axis for 3D non-reactive simulations.

be used, as shown in figure 12(c). The wrinkling factor in fresh gas is now quite reasonable but inside the reaction region, it is still almost 1, thus is useless to correct the unresolved turbulent flame speed. In fact, this is due to the high viscosity introduced by the high temperature in the flame region. To overcome this issue, a local fresh-gas weighted average process as in [37] is proposed. The wrinkling factor at $\vec{x} = \vec{x_0}$ inside the flame, is calculated by a weighted average of the factor inside a radius $r = (F + 1)\delta_l^0$ surrounding $\vec{x_0}$

$$\Xi(\vec{x_0}) = \frac{\iiint_{\|\vec{x}-\vec{x_0}\|\leq r} \Xi(\vec{x})\omega(\vec{x})d\mathcal{V}}{\iiint_{\|\vec{x}-\vec{x_0}\|\leq r} \omega(\vec{x})d\mathcal{V}} \tag{51}$$

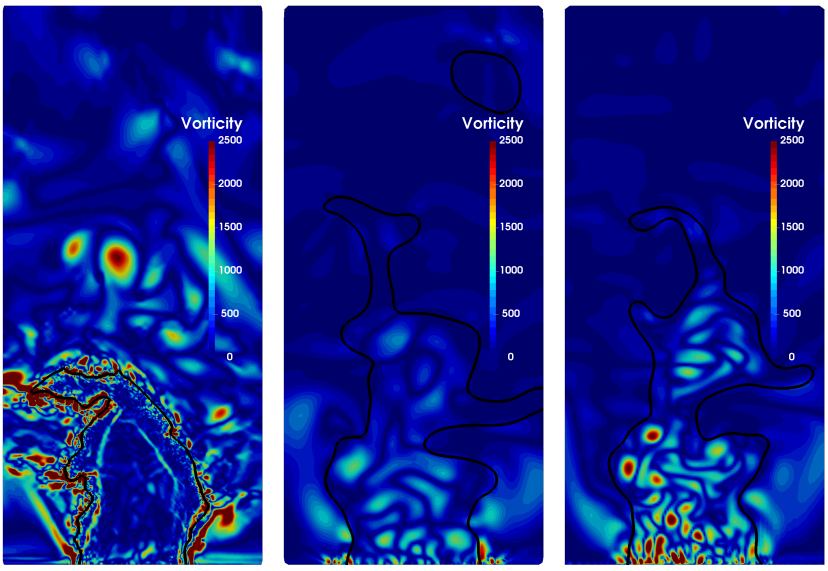

(a) MZ5-QL (b) UP5-TF_6-WF (c) $HYB_{0.03}$-TF_6-WF

Figure 11: Vorticity (1/s) fields for (I)LES of 2D simulations. The black lines indicate the flame front ($\widetilde{c} = 0.5$).

where the weight ω is evaluated such that only fresh gas is considered:

$$\omega(\vec{x}) = \begin{cases} 1 & \text{if } \widetilde{c}(\vec{x}) \leq 0.05 \\ 0 & \text{otherwise} \end{cases} \tag{52}$$

where $\widetilde{c}$ is the local resolved progress variable. After this treatment, the wrinkling factor inside the flame becomes reasonable, as shown in figure 12(d).

In figure 11(c), a snapshot of our best practice of TFLES is presented. One can see that with the low dissipative hybrid central-upwind scheme for Euler flux, OP_2 and fresh-gas weighted averaging for SGS wrinkling factor, this simulation resolves both the flow and the flame quite well.

3D simulations

The 3D simulations for reacting CH_4/air flame is performed based on 3D non-reacting and 2D reacting configurations. The mesh setup, turbulence injection strategy and boundary conditions are identical to non-reactive simulations Group II (last two columns of table 3). The numerical schemes for ILES is 5th order WENO-MZ scheme, with quasi-laminar approach for reaction terms (simulation MZ5-QL) and TFLES is performed at a thickening level $\mathcal{F} = 8$ with the hybrid central-upwind scheme (3% of upwind, simulation $HYB_{0.03}$-TF_8-WF). The local fresh gas average process in equation (51) is also applied for TFLES.

The instantaneous snapshots from this 3D simulations are as expected. The vorticity field in the fresh gas obtained in $HYB_{0.03}$-TF_8-WF (Fig. 13(a)) is quite close to the non-reactive simulations $HYB_{0.03}$-NR (Fig. 8(b)), and a reasonable wrinkling factor is achieved as shown in figure 13(c)[3]. However, the vorticity field in the fresh gas of MZ5-QL (Fig. 13(b)) is quite different from the non-reactive case. The vorticity field of MZ5-QL is quite oscillatory near the flame front, like in 2D reacting simulations.

Statistical results from experiments and this simulation are compared for both averaged progress variable and Flame Surface Density (FSD). The comparison of averaged progress variable can be achieved directly. However, the treatment for FSD should be performed with care, since the filtered variables obtained from TFLES can not be compared directly with experimental data. The experimental FSD can be easily obtained

[3]In 3D simulations, the wrinkling factor is only evaluated inside the reaction zone.

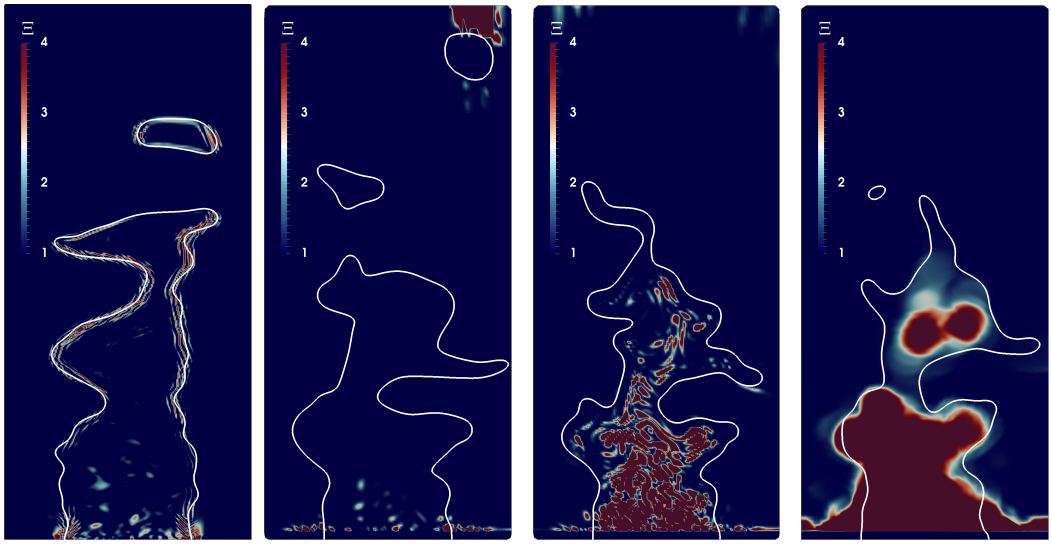

(a) UP5-TF$_6$-WF, Smagorinsky

(b) UP5-TF$_6$-WF,OP_2

(c) HYB$_{0.03}$-TF$_6$-WF, OP_2, no weighting

(d) HYB$_{0.03}$-TF$_6$-WF, OP_2, weighting

Figure 12: Wrinkling factor contour with different evaluation methods. The white lines are iso-value $\widetilde{c} = 0.5$ which indicate the flame front.

as

$$\mathrm{FSD}_E \equiv \|\nabla c_E\| \tag{53}$$

On the numerical side, LES gives the resolved progress variable $\widetilde{c_N}$. The resolved FSD is then

$$\mathrm{FSD}_N \equiv \|\nabla \widetilde{c_N}\| \tag{54}$$

Using the definition of the SGS wrinkling factor Ξ, one should have

$$\left\|\widetilde{\nabla c_N}\right\| = \Xi \|\nabla \widetilde{c_N}\| = \Xi \cdot \mathrm{FSD}_N \tag{55}$$

Concerning equation (53), the two comparable variables should be the filtered experimental flame surface density $\widetilde{\mathrm{FSD}_E}$, and $\Xi \cdot \mathrm{FSD}_N$ in simulations. But the LES filter is difficult to define, especially for TFLES [38]. At this stage, a Gaussian filter with the same filter size as the simulation grid size Δ_x is taken to perform the filtering process for experimental results. More details on the post treatment for the experimental tomographies can be found in [3].

The mean progress variable and FSD from this 3D simulation and experiments are compared along the jet axis in figure 14. The results of the simulation are averaged azimuthally over 35 ms after the flame is statistically stable. It is clear that TFLES catches much better flame location and structure than ILES does. The FSD given by TFLES along the jet axis is higher than in experiments, whereas the MZ5-QL ILES provides the proper FSD but with a too short flame. This is clearly due to excessive laminar flame speed produced by ILES at this grid resolution as shown in the 1D laminar flame test case.

The mean progress variable and FSD on the jet axis cut-plane are also displayed in figure 15 and 16. Compared to the experimental results (left half of each picture), both simulations give reasonable flame length and flame surface density. However, HYB$_{0.03}$-TF$_8$-WF with the subgrid scale wrinkling model from [5] shows a better agreement with the experiment.

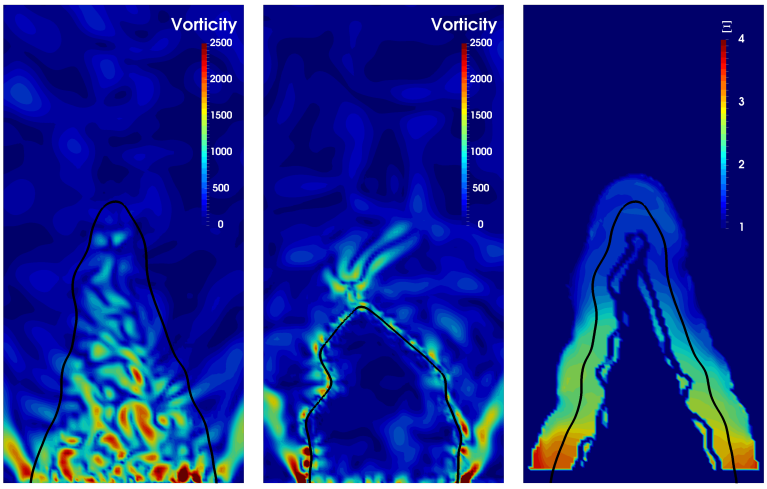

(a) $HYB_{0.03}$-TF_8-WF, vorticity (b) MZ5-QL, vorticity (c) $HYB_{0.03}$-TF_8-WF, SGS wrinkling factor

Figure 13: Vorticity (1/s) field and SGS wrinkling factor of 3D reactive simulations on the jet axis cut-plane. The black line ($\widetilde{c} = 0.5$) indicates the flame front.

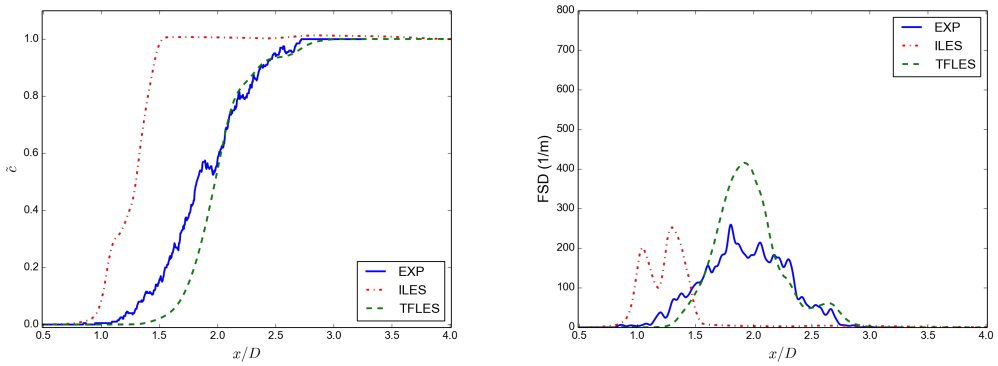

(a) Mean progress variable (b) Mean flame surface density

Figure 14: Mean Progress Variable and FSD curve along the jet axis for 3D reacting simulations

4 Conclusions

In this work, a fully compressible N-S solver with ASR low-Mach modifications has been applied to ILES and TFLES of low-speed premixed turbulent combustion. ILES with non-linear WENO shock-capturing schemes can provide acceptable results compared to the experiment provided the grid size is of the order of one flame thickness. However, the mechanism for reasonable flame speed comes from an increased laminar flame speed instead of a proper turbulent flame surface density. TFLES is achieved by combining the explicit SGS model from [5] for combustion and implicit SGS turbulence modeling from hybrid central-upwind spatial schemes. In this approach, a careful examination of the explicit SGS model inputs, and of the ILES flow field resolution is mandatory.

Acknowledgments This work was granted access to the HPC resources of IDRIS under the allocations 2014-2b0913 and 2015-2b0913 made by GENCI (Grand Equipement National de Calcul Intensif). Song Zhao's fellowship is provided by the French Government's Investissement d'Avenir program: Laboratoire d'Excellence CAPRYSSES (Grant No. ANR-11-LABX-0006-01).

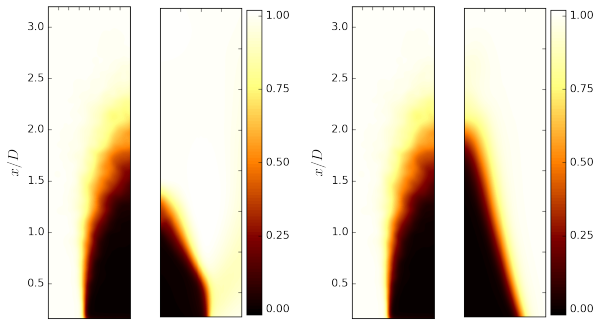

(a) MZ5-QL (b) $\mathrm{HYB}_{0.03}$-TF_8-WF

Figure 15: Mean progress variable of 3D reacting simulations. Experimental and simulation results are plotted on the left and on the right half of each figure, respectively.

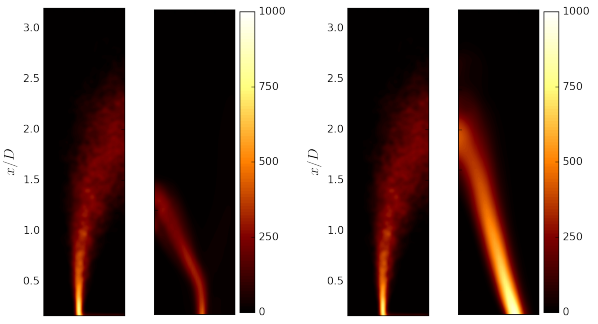

(a) MZ5-QL (b) $\mathrm{HYB}_{0.03}$-TF_8-WF

Figure 16: Mean flame surface density (1/m) of 3D reacting simulations. Experimental and simulation results are plotted on the left and on the right half of each figure, respectively.

Appendix

$$\Lambda = \begin{pmatrix} u - c/\alpha & & & & & & & \\ & u & & & & & & \\ & & u & & & & & \\ & & & u & & & & \\ & & & & u + c/\alpha & & & \\ & & & & & u & & \\ & & & & & & \ddots & \\ & & & & & & & u \end{pmatrix} \tag{56}$$

with

$$c \equiv \sqrt{\gamma r T}$$

$$R^{-1} = \begin{pmatrix} L_{10} & -\frac{(\gamma-1)\alpha^2 u + \alpha c}{2c^2} & -\frac{(\gamma-1)\alpha^2 v}{2c^2} & -\frac{(\gamma-1)\alpha^2 w}{2c^2} & \frac{(\gamma-1)\alpha^2}{2c^2} & L_{11} & \cdots & L_{1N_{sp}} \\ L_{20} & \frac{(\gamma-1)\alpha^2 u}{c^2} & \frac{(\gamma-1)\alpha^2 v}{c^2} & \frac{(\gamma-1)\alpha^2 w}{c^2} & -\frac{(\gamma-1)\alpha^2}{c^2} & -2L_{11} & \cdots & -2L_{1N_{sp}} \\ -\frac{v}{\rho} & 0 & \frac{1}{\rho} & 0 & 0 & 0 & \cdots & 0 \\ -\frac{w}{\rho} & 0 & 0 & \frac{1}{\rho} & 0 & 0 & \cdots & 0 \\ L_{30} & -\frac{(\gamma-1)\alpha^2 u - \alpha c}{2c^2} & -\frac{(\gamma-1)\alpha^2 v}{2c^2} & -\frac{(\gamma-1)\alpha^2 w}{2c^2} & \frac{(\gamma-1)\alpha^2}{2c^2} & L_{11} & \cdots & L_{1N_{sp}} \\ -\frac{Y_1}{\rho} & 0 & 0 & 0 & 0 & \frac{1}{\rho} & \cdots (0) & 0 \\ \vdots & \vdots & \vdots & \vdots & \vdots & 0 & \ddots & \vdots \\ -\frac{Y_{N_{\mathrm{sp}}}}{\rho} & 0 & 0 & 0 & 0 & 0 & \cdots & \frac{1}{\rho} \end{pmatrix} \tag{57}$$

with

$$\kappa \equiv \frac{u^2 + v^2 + w^2}{2}$$

$$L_{10} = \frac{\alpha c u + (\gamma - 1)\,\alpha^2 \kappa + (1 - \gamma)\,\alpha^2 h + \alpha^2 c^2}{2c^2}$$

$$L_{20} = -\frac{(\gamma - 1)\,\alpha^2 \kappa + (1 - \gamma)\,\alpha^2 h + \left(\alpha^2 - 1\right) c^2}{c^2}$$

$$L_{30} = -\frac{\alpha c u + (1 - \gamma)\,\alpha^2 \kappa + (\gamma - 1)\,\alpha^2 h - \alpha^2 c^2}{2c^2}$$

$$L_{1k} = \frac{\gamma r_k \alpha^2 T + (\gamma - 1)\,\alpha^2 h - \alpha^2 c^2 + (1 - \gamma)\,h_k \alpha^2}{2c^2}$$

$$R = \begin{pmatrix} 1 & 1 & 0 & 0 & 1 & 0 & \cdots & 0 \\ u - \frac{c}{\alpha} & u & 0 & 0 & u + \frac{c}{\alpha} & 0 & \cdots & 0 \\ v & v & \rho & 0 & v & 0 & \cdots & 0 \\ w & w & 0 & \rho & w & 0 & \cdots & 0 \\ R_{50} & \kappa + h - \frac{c^2}{\gamma - 1} & \rho v & \rho w & \kappa + h + u\frac{c}{\alpha} + \frac{(1-\alpha^2)c^2}{(\gamma-1)\alpha^2} & R_{51} & \cdots & R_{5N_{sp}} \\ Y_1 & Y_1 & 0 & 0 & Y_1 & \rho & \cdots (0) & 0 \\ \vdots & \vdots & 0 & 0 & \vdots & \vdots (0) & \ddots & \vdots \\ Y_{N_{\rm sp}} & Y_{N_{\rm sp}} & 0 & 0 & Y_{N_{\rm sp}} & 0 & \cdots & \rho \end{pmatrix} \tag{58}$$

with

$$R_{50} = \kappa + h - u\frac{c}{\alpha} + \frac{(1-\alpha^2)c^2}{(\gamma-1)\alpha^2}$$

$$R_{5k} = -\frac{\gamma r_k \rho T + \left((\gamma-1)\,h - c^2 + (1-\gamma)\,h_k\right)\rho}{\gamma - 1}$$

References

[1] N. Mazellier, B. Danaila, and B. Renou. Multi-scale injection: a new tool to generate intense homogeneous and isotropic turbulence for premixed combustion. *Journal of Turbulence*, 11(43):1–30, 2010.

[2] R. Fragner, N. Mazellier, F. Halter, C. Chauveau, and I. Gökalp. Multi-scale high intensity turbulence generator applied to a high pressure turbulent burner. *Flow, Turbulence and Combustion*, 94(1):263–283, 2015.

[3] F. Thiesset, G. Maurice, F. Halter, N. Mazellier, C. Chauveau, and I. Gökalp. Geometrical properties of turbulent premixed flames and other corrugated interfaces. *Phys. Rev. E*, 93:013116, Jan 2016.

[4] T. Poinsot and D. Veynante. *Theoretical and Numerical Combustion*. 2nd edition. Edwards, 2005.

[5] F. Thiesset, G. Maurice, F. Halter, N. Mazellier, C. Chauveau, and I. Gökalp. Modeling of the subgrid scale wrinkling factor for large-eddy simulation of turbulent premixed combustion. *Combustion Theory and Modelling*, 2016.

[6] A. Burcat and B. Ruscic. Ideal gas thermodynamic data in polynomial form for combustion and air pollution use, December 2006. Third Millennium Ideal Gas and Condensed Phase Thermochemical Database for Combustion [on line database].

[7] A. Ern and V. Giovangigli. Fast and accurate multicomponent transport property evaluation. *Journal of Computational Physics*, 120(1):105 – 116, 1995.

[8] A. Ern and V. Giovangigli. Eglib: A general-purpose fortran library for multicomponent transport property evaluation. *Manual of EGlib*, (3):12, 2004.

[9] A. Ern and V. Giovangigli. *Multicomponent transport algorithms*, volume 24. Springer, 1994.

[10] R.J. Kee, F.M. Rupley, J.A. Miller, M.E. Coltrin, J.F. Grcar, E. Meeks, H.K. Moffat, A.E. Lutz, G. Dixon-Lewis, M.D. Smooke, J. Warnatz, G.H. Evans, R.S. Larson, R.E. Mitchell, L.R. Petzold, W.C. Reynolds, M. Caracotsios, W.E. Stewart, and P. Glarborg. *CHEMKIN collection*. release 3.5. Reaction Design, Inc., San Diego, CA, 1999.

[11] David G. Goodwin, Harry K. Moffat, and Raymond L. Speth. Cantera: An object-oriented software toolkit for chemical kinetics, thermodynamics, and transport processes, 2015. Version 2.2.0.

[12] S. B. Pope. *Turbulent flows*. Cambridge university press, 2000.

[13] P. Sagaut. *Large-Eddy Simulation for Incompressible Flows*. 3rd edition. Springer, Berlin, 2006.

[14] E. Garnier, N. Adams, and P. Sagaut. *Large Eddy Simulation for Compressible Flows*. Scientific Computations. Springer, 2009.

[15] G. Wang, M. Boileau, and D. Veynante. Implementation of a dynamic thickened flame model for large eddy simulations of turbulent premixed combustion. *Combustion and Flame*, 158:2199–2213, 2011.

[16] B. Fiorina, D. Veynante, and S. Candel. Modeling combustion chemistry in large eddy simulation of turbulent flames. *Flow, Turbulence and Combustion*, 94(1):3–42, 2015.

[17] F.F. Grinstein, L.G. Margolin, and W.J. Rider. *Implicit Large Eddy Simulation : computing turbulent fluid dynamics*. Cambridge University Press, 2007.

[18] S. Hickel, N. A. Adams, and J. A. Domaradzki. An adaptive local deconvolution method for implicit LES. *Journal of Computational Physics*, 213(1):413–436, March 2006.

[19] J.P. Boris, F.F. Grinstein, E.S. Oran, and R.L Kolbe. New insights into large eddy simulation. *Fluid Dynamics Research*, 10:199–228, 1992.

[20] E. Garnier, M. Mossi, P. Sagaut, P. Comte, and M. Deville. On the use of shock-capturing schemes for large-eddy simulation. *Journal of Computational Physics*, 153:273–311, 1999.

[21] M. Karaca, N. Lardjane, and I. Fedioun. Implicit large eddy simulation of high-speed non-reacting and reacting air/h_2 jets with a 5th order weno scheme. *Computers & Fluids*, 62:25–44, 2012.

[22] S. Zhao, N. Lardjane, and I. Fedioun. Comparison of improved finite-difference WENO schemes for the implicit large eddy simulation of turbulent non-reacting and reacting high-speed shear flows. *Computers & Fluids*, 95:74–87, 2014.

[23] P.J. O'Rourke and F.V. Bracco. Two scaling transformations for the numerical computation of multidimensional unsteady laminar flames. *Journal of Computational Physics*, 33(2):185–203, 1979.

[24] O. Colin, F. Ducros, D. Veynante, and T. Poinsot. A thickened flame model for large eddy simulations of turbulent premixed combustion. *Physics of Fluids*, 12(7):1668–1693, 2000.

[25] F. Thiesset, G. Maurice, F. Halter, N. Mazellier, C. Chauveau, and I. Gökalp. Modelling of the subgrid scale wrinkling factor

for large-eddy simulation of turbulent premixed combustion. In *15th International Conference on Numerical Combustion*, Avignon, France, 19-22 April 2015, 2015.

[26] F. Charlette, C. Meneveau, and D. Veynante. A power-law flame wrinkling model for LES of premixed turbulent combustion. Part I. *Combustion and Flame*, 131:159–180, 2002.

[27] E.R. Hawkes, O. Chatakonda, H. Kolla, A.R. Kerstein, and J.H. Chen. A petascale direct numerical simulation study of the modelling of flame wrinkling for large-eddy simulations in intense turbulence. *Combustion and flame*, 159:2690–2703, 2012.

[28] J. Smagorinsky. General circulation experiments with the primitive equations i. the basic experiment. *Monthly Weather Review*, 91(3):99–164, 1963.

[29] C.W. Shu. Essentially non-oscillatory and weighted essentially non-oscillatory schemes for hyperbolic conservation laws. Technical Report NASA/CR-97-206253, ICASE report No.97-65, Langley Research Center, November 1997.

[30] Philip L Roe. Approximate riemann solvers, parameter vectors, and difference schemes. *Journal of computational physics*, 43(2):357–372, 1981.

[31] A.K. Henrick, T.D. Aslam, and J.M. Powers. Mapped weighted essentially non-oscillatory schemes: Achieving optimal order near critical points. *Journal of Computational Physics*, 207:542–567, 2005.

[32] R. Borges, M. Carmona, B. Costa, and W.S. Don. An improved weighted essentially non-oscillatory scheme for hyperbolic conservation laws. *Journal of Computational Physics*, 227:3191–3211, 2008.

[33] L. Zhao, Y. Zhang, and C. Haixin. A low dissipation numerical scheme for Implicit Large Eddy Simulation. *Computers & Fluids*, 117:233–246, 2015.

[34] Y. Wang and A. Trouvé. Artificial Acoustic Stiffness Reduction in Fully Compressible, Direct Numerical Simulation of Combustion. *Combustion Theory and Modelling*, 8(3), 2004.

[35] J.O. Hinze. *Turbulence, 2nd edition.* Mc Graw Hill, 1975.

[36] M. Lesieur. *Turbulence in Fluids, Fourth edition.* Fluid mechanics and its applications, Vol. 84. Springer, 2008.

[37] D. Veynante and V. Moureau. Analysis of dynamic models for large eddy simulations of turbulent premixed combustion. *Combustion and Flame*, 162(12):4622–4642, 2015.

[38] R. Mercier, V. Moureau, D. Veynante, and B. Fiorina. LES of turbulent combustion: On the consistency between flame and flow filter scales. *Proceedings of the Combustion Institute*, 35(2):1359–1366, 2015.